



**HAL**  
open science

## **Magneto-ionics in annealed W/CoFeB/HfO<sub>2</sub> thin films**

Rohit Pachat, Djoudi Ourdani, Maria-andromachi Syskaki, Alessio Lamperti, Subhajit Roy, Song Chen, Adriano Di Pietro, Ludovic Largeau, Roméo Juge, Maryam Massouras, et al.

► **To cite this version:**

Rohit Pachat, Djoudi Ourdani, Maria-andromachi Syskaki, Alessio Lamperti, Subhajit Roy, et al.. Magneto-ionics in annealed W/CoFeB/HfO<sub>2</sub> thin films. *Advanced Materials Interfaces*, 2022, 9 (36), pp.2200690. 10.1002/admi.202200690 . hal-03787337

**HAL Id: hal-03787337**

**<https://hal.science/hal-03787337>**

Submitted on 7 Nov 2022

**HAL** is a multi-disciplinary open access archive for the deposit and dissemination of scientific research documents, whether they are published or not. The documents may come from teaching and research institutions in France or abroad, or from public or private research centers.

L'archive ouverte pluridisciplinaire **HAL**, est destinée au dépôt et à la diffusion de documents scientifiques de niveau recherche, publiés ou non, émanant des établissements d'enseignement et de recherche français ou étrangers, des laboratoires publics ou privés.



Distributed under a Creative Commons Attribution - NonCommercial 4.0 International License

# Magneto-Ionics in Annealed W/CoFeB/HfO<sub>2</sub> Thin Films

Rohit Pachat, Djoudi Ourdani, Maria-Andromachi Syskaki, Alessio Lamperti, Subhajit Roy, Song Chen, Adriano Di Pietro, Ludovic Largeau, Roméo Juge, Maryam Massouras, Cristina Balan, Johannes Wilhelmus van der Jagt, Guillaume Agnus, Yves Roussigné, Mihai Gabor, Salim Mourad Chérif, Gianfranco Durin, Shimpei Ono, Jürgen Langer, Damien Querlioz, Dafiné Ravelosona, Mohamed Belmeguenai, and Liza Herrera Diez\*

The magneto-ionic modulation of the Dzyaloshinskii–Moriya interaction (DMI) and the perpendicular magnetic anisotropy (PMA), in W/CoFeB/HfO<sub>2</sub> stacks annealed at different temperatures and for varying annealing times, are presented in this work. A large modulation of PMA and DMI is observed in the systems annealed at 390 and 350 °C, whereas no response to voltage is observed in the as-grown samples. A strong DMI is only observed in the samples annealed at 390 °C for 1 h, while PMA is present for all annealing times at temperatures of 390 and 350 °C. Magnetic properties including domain wall velocity improve drastically with increasing the annealing temperature and time, while the magneto-ionic reversibility is increasingly compromised. The changes in PMA and DMI induced by the gate voltages in the samples annealed at 390 °C are permanent, while partial reversibility is only observed for the samples annealed at 350 °C for short times. This dependence of reversibility on post-grown annealing has been associated to the influence of crystallization on ion mobility. These results show that a compromise between the enhancement of the magnetic properties and the magneto-ionic performance could be needed in systems requiring annealing to develop PMA and DMI.

## 1. Introduction

Electric field control of magnetic properties in ferromagnetic (FM) thin films is a sought-after feature for spintronics devices, as it offers great potential for high energy efficiency in memory applications. In particular, the electric field-induced charge accumulation at FM interfaces has been shown to induce significant changes in perpendicular magnetic anisotropy (PMA), domain wall (DW) motion,<sup>[1–3]</sup> and in the Dzyaloshinskii–Moriya interaction (DMI).<sup>[4, 5]</sup> However, the changes induced by conventional charge accumulation are limited by electrostatic screening<sup>[6]</sup> and are also volatile, meaning that these changes revert to their initial state when the electric field is turned off. In this regard, magneto-ionics,<sup>[7]</sup> where the electric field can modify the oxidation state of FM materials, can not only offer large variations in

R. Pachat, S. Roy, L. Largeau, M. Massouras, G. Agnus, D. Querlioz, D. Ravelosona, L. Herrera Diez  
Centre de Nanosciences et de Nanotechnologies  
CNRS  
Université Paris-Saclay  
Palaiseau 91120, France  
E-mail: liza.herrera-diez@c2n.upsaclay.fr  
D. Ourdani, Y. Roussigné, S. M. Chérif, M. Belmeguenai  
Laboratoire des Sciences des Procédés et des Matériaux  
CNRS-UPR 3407  
Université Sorbonne Paris Nord  
Villetaneuse 93430, France  
M.-A. Syskaki, J. Langer  
Singulus Technology AG  
Hanauer Landstrasse 103 63796, Kahl am Main, Germany

A. Lamperti  
IMM-CNR  
Unit of Agrate Brianza  
Via C. Olivetti 2, Agrate Brianza 20864, Italy  
S. Chen, R. Juge, J. W. van der Jagt, D. Ravelosona  
Spin-Ion Technologies  
10 Boulevard Thomas Gobert, Palaiseau 91120, France  
A. D. Pietro, G. Durin  
Istituto Nazionale di Ricerca Metrologica  
Strada delle Cacce 91, Torino 10135, Italy  
A. D. Pietro  
Politecnico di Torino  
Viale duca degli Abruzzi 24, Torino 10129, Italy  
C. Balan  
Univ. Grenoble Alpes, CNRS, Institut Néel  
Grenoble 38000, France  
M. Gabor  
Center for Superconductivity  
Spintronics and Surface Science  
Physics and Chemistry Department  
Technical University of Cluj-Napoca  
Cluj-Napoca RO-400114, Romania  
S. Ono  
Central Research Institute of Electric Power Industry  
Yokosuka, Kanagawa 240-0196, Japan

 The ORCID identification number(s) for the author(s) of this article can be found under <https://doi.org/10.1002/admi.202200690>.

© 2022 The Authors. Advanced Materials Interfaces published by Wiley-VCH GmbH. This is an open access article under the terms of the Creative Commons Attribution-NonCommercial License, which permits use, distribution and reproduction in any medium, provided the original work is properly cited and is not used for commercial purposes.

DOI: 10.1002/admi.202200690

**Table 1.** Annealing parameters of samples S1 to S4.

Sample	Ramp-up duration [min]	Annealing temperature [°C]	Dwell time [min]
S1	17	350	60
S2	22	390	60
S3	140	350	0
S4	140	390	0

magnetic properties but also provide non-volatility. Magneto-ionic effects and functionalities that have been demonstrated include an electric field-induced spin reorientation transition (SRT) between PMA and in-plane anisotropy,<sup>[8]</sup> efficient domain wall traps,<sup>[9]</sup> control of saturation magnetization,<sup>[10]</sup> DMI<sup>[11]</sup> and the control of the spin accumulation direction for spin-orbit torques.<sup>[12]</sup> Recently, several works have focused on exploring the use of different types of ions<sup>[8,10,13]</sup> and FM/oxide interfaces<sup>[14]</sup>, as well as on modulating the degree of oxidation at FM/oxide interfaces<sup>[15,16]</sup> to control magnetic properties and gain insight into the magneto-ionic mechanism.

The impact of post-growth annealing, which is vital to achieving robust magnetic properties in CoFeB-based materials through crystallization,<sup>[17]</sup> on magneto-ionics has only begun to spark an interest. In Ta/CoFeB/HfO<sub>2</sub>, post-growth annealing has shown to critically reduce the speed of the magneto-ionic response,<sup>[15]</sup> which has been attributed to a potentially lower ion mobility in crystallized systems compared to their amorphous counterpart. It is therefore of importance to characterize magneto-ionics in annealed CoFeB systems to optimize both the magnetic properties of the films and their magneto-ionic performance. W/CoFeB-based systems are known to exhibit DMI and PMA, as well as a large spin Hall angle in the  $\beta$ -phase of W,<sup>[18–20]</sup> which makes them very attractive for spintronics applications. In these systems, post-growth annealing is systematically used to enhance DMI, and PMA,<sup>[18]</sup> which in W/CoFeB/MgO is associated with the crystallization of CoFeB.<sup>[21]</sup> In addition, oxygen incorporation into W/CoFeB/MgO has been used to enhance spin-orbit torques.<sup>[22]</sup> Therefore, the characterization of the magneto-ionic response using oxygen species in annealed W/CoFeB/HfO<sub>2</sub> stacks is of significant interest.

In this study, we investigate the magneto-ionic response in as-grown and annealed W/CoFeB/HfO<sub>2</sub> stacks. We show a large magneto-ionic modulation of DMI and PMA in W/CoFeB/HfO<sub>2</sub> annealed at 390 °C, where the gate-voltage-induced oxidation of Fe and Co has been confirmed by X-ray photoelectron spectroscopy (XPS). The oxygen 1s XPS signal after voltage exposure reveals the presence of an additional peak at higher binding energies that can be attributed to the oxygen species introduced in the system through gating. This system shows no reversibility within the gate voltage window explored, which is likely a result of a lower ion mobility in the CoFeB layer after the crystallization induced by high temperature annealing. The samples annealed at 350 °C, on the other hand, show a partially reversible SRT induced by the gate voltage, however, the DMI is greatly reduced and the domain wall velocity is significantly lower than in the sample annealed at 390 °C. Finally, the gate voltage did not induce any observable changes in magnetic

anisotropy in the as-grown samples, which present neither PMA nor DMI.

Our results show that a compromise between the annealing temperature and the magneto-ionic performance could be needed to allow for a balance between the enhancement of magnetic properties and a good magneto-ionic performance.

## 2. Results and Discussion

The magnetic stack used in this study is W (4 nm)/Co<sub>20</sub>Fe<sub>60</sub>B<sub>20</sub> (1 nm)/HfO<sub>2</sub> (3 nm) grown by magnetron sputtering (see the Experimental Section). The samples were annealed at 350 and 390 °C using either a temperature program with a 140 min ramp-up time and zero dwelling time at the target temperature, or a short ramp-up time (17 or 22 min) and a 60 min dwelling time at the target temperature. The annealing conditions corresponding to each of the different samples studied (S1, S2, S3, and S4) are summarized in Table 1. W is in the polycrystalline  $\beta$ -phase ( $\beta$ -W), and CoFeB and HfO<sub>2</sub> are amorphous in the as-grown state. The phases of W and HfO<sub>2</sub> after annealing remained unchanged in all cases, which was confirmed by grazing incident X-ray diffraction (see Section S1, Supporting Information). The peaks of CoFeB were not observed due to the detection limit of the diffractometer. All annealed samples in our study show PMA. A schematic of the device is shown in Figure 1a.

As-grown samples have an in-plane easy magnetization axis. PMA in CoFeB/oxide based heterostructures can arise due to the 2p-3d hybridization between orbitals from oxygen and the ferromagnet. This contribution to PMA is dominant, for example, in the archetypal Ta/CoFeB/MgO stacks and in Pt/Co/AlOx systems<sup>[23]</sup> and can be exploited to induce PMA through magneto-ionic control of the oxidation level at the FM/oxide interface.<sup>[11,15]</sup> In the present case, neither positive (+4 V) nor negative gate voltages (−2.3, −2.5, and −3 V) produced an

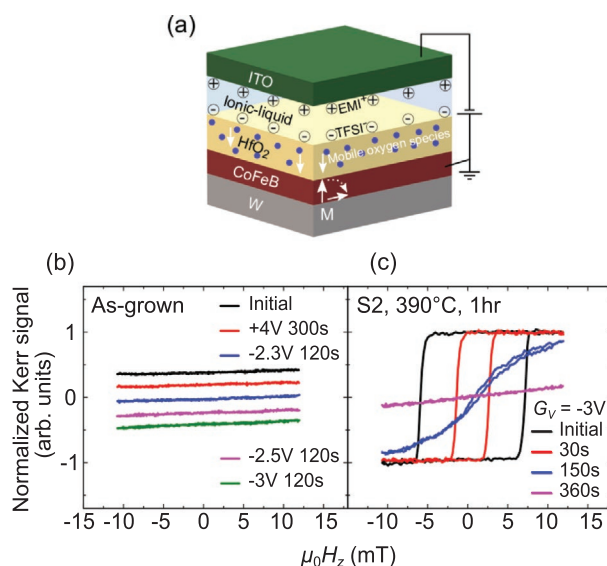


**Figure 1.** a) Schematic of the structure of the ionic-liquid gate device and pMOKE signal under an out-of-plane magnetic field ( $\mu_0 H_z$ ) of the b) as-grown, and c) annealed S2 sample under different gate voltages and gating times.

out-of-plane (OOP) signature in pMOKE for the as-grown samples, as shown in Figure 1b. In contrast, in other liquid-gated systems based on Pt/Co/HfO<sub>2</sub> and Ta/CoFeB/HfO<sub>2</sub>, the under-oxidized as-grown state shows PMA after application of similar negative voltages, due to the controlled oxidation of the FM/oxide interface.<sup>[11,15]</sup> It has been shown that a significant contribution to PMA can also arise from the heavy-metal (HM)/FM interface which depends on factors such as the 5d–3d hybridization of the heavy metal and ferromagnet's orbitals, interface intermixing and interface structure.<sup>[18,21,24]</sup> The contribution of the HM/FM interface to PMA has been found to be particularly important in W/CoFeB/MgO systems, including a significant dependence of PMA on the W crystalline phase.<sup>[18]</sup> In these systems there is also a need of thermal annealing at minimum temperatures close to 250 °C to obtain PMA.<sup>[18,24]</sup> The importance of the W/CoFeB interface contribution to PMA, and its link to thermal annealing, is the base of our interpretation of the lack of magneto-ionic response in as-grown W/CoFeB/HfO<sub>2</sub>. A gate-controlled oxidation at the CoFeB/HfO<sub>2</sub> interface alone does not induce PMA in our system, thermal annealing is still a necessary step. In the following, we will discuss the magneto-ionic response in samples annealed under different conditions (S1 to S4), where PMA is present in the initial state, before the application of gate voltages.

A gate voltage of –3 V applied to S2 (annealing at 390 °C for 1 h) can progressively drive the magnetization from OOP to in-plane (IP) after a total exposure time of 360 s, as shown in Figure 1c. The evolution of the surface DMI ( $D_s$ ) as a function of the gating time was extracted from Brillouin light scattering (BLS) spectroscopy measurements (see Section S4, Supporting Information) and is shown in Figure 2. It is represented as  $D_s = D \cdot t$ , where  $D$  and  $t$  are the effective DMI constant and the thickness of the CoFeB layer, respectively. The corresponding variations in  $M_s \cdot t$  are shown in the inset, where  $M_s$  is the saturation magnetization. The positive sign of  $D_s$  in our system indicates a right-handed chirality, as reported in other W/CoFeB systems.<sup>[18,25]</sup>  $D_s$  shows a sharp decrease from the 0.62 pJ m<sup>-1</sup> measured before exposure to the gate voltage down to 0.06 pJ m<sup>-1</sup> after a

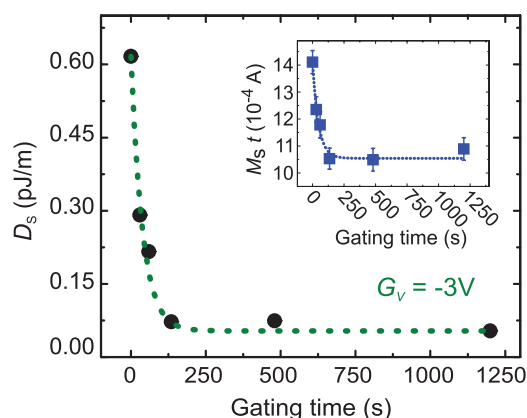


**Figure 2.** Surface DMI constant ( $D_s$ ) as a function of the gating time under a gate voltage  $G_V = -3$  V in sample S2. The inset shows the corresponding changes in  $M_s \cdot t$ , where  $M_s$  is the saturation magnetization and  $t$  the thickness of the film, respectively. The error bars represent the noise amplitude of the measurement. The dotted lines are a guide to the eye.

gating time of 135 s. After this point, no significant variations are observed for longer gating times. This gate-voltage-induced decrease in  $D_s$  corresponds to a variation by a factor of ten that accompanies the SRT shown in Figure 1c.  $M_s \cdot t$  shows a similar profile, where the loss of magnetic moment could be attributed to the oxidation of Fe and Co, due to the migration of oxygen species. Ion migration is also at the origin of the decrease in DMI, since it could result in a decoupling between the W and CoFeB layers as already proposed for Pt/Co/HfO<sub>2</sub>/IL devices.<sup>[11]</sup>

In order to probe the changes in the chemical environment of the CoFeB/HfO<sub>2</sub> interface, XPS measurements were performed before and after annealing and after exposure to gate voltages (see the Experimental Section). Figure 3 shows the XPS spectra of Fe 2p<sub>3/2</sub> and 2p<sub>1/2</sub>, Co 2p<sub>3/2</sub> and 2p<sub>1/2</sub>, and O 1s of as-grown, S2 and S2 exposed to –3 V for 30 and 480 s at the CoFeB/HfO<sub>2</sub> interface. As shown in Figure 3a,b, the Fe 2p and Co 2p peaks show no significant differences between the as-grown and S2 samples, confirming the metallic nature of Fe and Co before and after annealing, and therefore indicating that PMA in S2 does not originate from the oxidation of the CoFeB/HfO<sub>2</sub> interface, as discussed earlier. A similar scenario is observed for O 1s, where minor changes are detected before and after annealing. This is well in line with the absence of PMA in the as-grown samples for the entire negative gate voltage range, as shown in Figure 1b, which supports a scenario where the properties of the HM/FM interface are the key to inducing PMA in our system.

The 2p peaks of Fe and Co shift toward higher binding energies in S2 samples exposed to –3 V, indicating the transition of Fe and Co to higher valence states.<sup>[11,26]</sup> In the case of Fe, the presence of Fe oxides such as Fe<sub>2</sub>O<sub>3</sub> and Fe<sub>3</sub>O<sub>4</sub> is well indicated by the XPS lines at binding energies in the vicinity of 710 and 724 eV,<sup>[27]</sup> as shown in Figure 3a. Co also shows a strong signature of oxidation with XPS peaks appearing at 782 and 790 eV.<sup>[28]</sup> The XPS O 1s profile shown in Figure 3c for the as-grown sample and S2 contains a prominent broad peak near 530 eV and a less pronounced peak near 532 eV. The peak near 530 eV is compatible with the signature of oxygen in HfO<sub>2</sub>, and both Fe and Co oxides.<sup>[27–29]</sup> The peak at higher binding energies becomes dominant after the application of the gate voltage, and can therefore be related to the mobile oxygen species that migrate under the action of the gate voltage. A possible scenario is that this signal corresponds to Fe and Co hydroxide species formed by combination with water molecules from the atmosphere, which have been reported to show XPS peaks near 531–532 eV.<sup>[27,28]</sup> This signal can also contain a contribution of non-dissociated H<sub>2</sub>O molecules.<sup>[30]</sup>

Positive voltages up to +4 V do not produce any significant changes in the magnetic state achieved after the application of –3 V in S2. Samples S1 (annealing at 350 °C for 1 h) and S4 (annealing at 390 °C with zero dwell time) show a similar magneto-ionic response as S2, negative voltages irreversibly drive the magnetization from OOP to IP (see Sections S2 and S3, Supporting Information). Only sample S3 (annealing at 350 °C with zero dwell time) showed limited reversibility under positive voltages, as shown in Figure 4. This progressive suppression of reversibility is attributed to an increase of thermally induced crystallization in W/CoFeB/HfO<sub>2</sub> at higher annealing

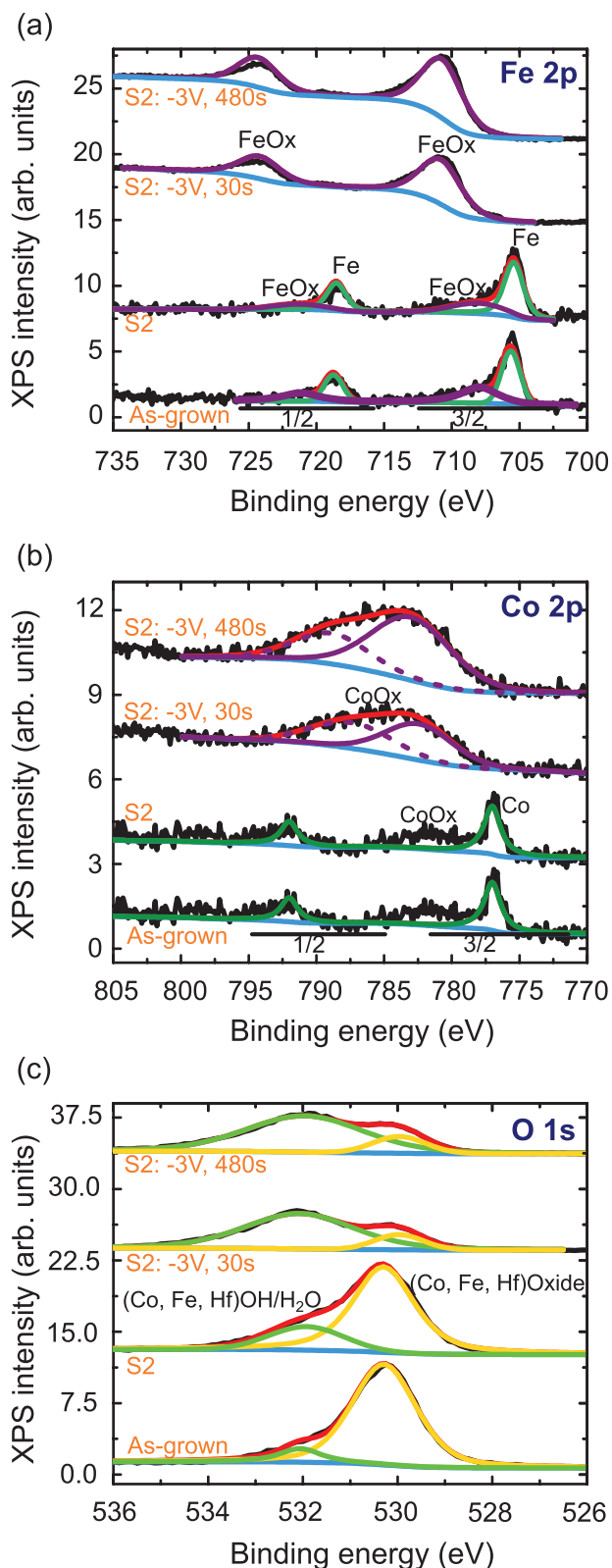


**Figure 3.** XPS spectra of a) Fe  $2p_{3/2}$  and  $2p_{1/2}$ , b) Co  $2p_{3/2}$  and  $2p_{1/2}$ , and c) O 1s for as-grown samples, S2, and S2 exposed to  $-3$  V for 30 and 480 s. Raw data (black), total fitting (red), background (blue), and fitting of each peak: light green and yellow for O 1s peaks; dark green for Co and Fe 2p, and purple (dashed and solid) for oxides of Fe and Co 2p.

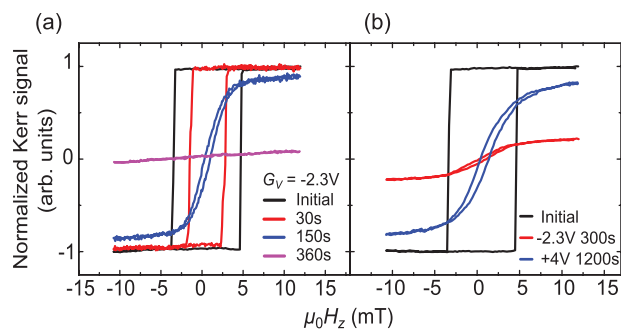


**Figure 4.** pMOKE hysteresis loops measured in sample S3 ( $350$  °C, zero dwell time) showing an SRT induced by the exposure to a gate voltage of  $-2.3$  V for a) 360 s, and b) partial reversibility of the IP magnetized state after exposure to  $+4$  V for 1200 s.

temperatures and longer annealing times, in analogy to what has been reported for W/CoFeB/MgO systems in the annealing temperature window between  $300$  and  $400$  °C.<sup>[31]</sup> In addition, the gate voltage required to reorient the magnetization easy axis from OOP to IP in S3 is  $-2.3$  V, a lower value compared to the  $-3$  V necessary to observe an SRT in S2, for the same gating time. This also supports the hypothesis of a more favorable ionic diffusion in samples that are closer to an amorphous state, where ionic conduction channels are not limited to the grain boundaries, as could be expected in granular systems.<sup>[32]</sup>

Although lower annealing temperatures could be explored to achieve full reversibility, the DMI in sample S3, has already been found to be significantly lower than that of S2. The frequency shift measured by BLS is negligible in this sample compared to the shift of about  $1$  GHz measured at  $k = 20$   $\mu\text{m}^{-1}$  in S2 (see Section S4, Supporting Information). This presents the need of a compromise between the magneto-ionic performance and the enhancement of the magnetic properties of the film. DMI is a key aspect in this compromise since it is of critical importance for the design of materials hosting chiral magnetic structures such as skyrmions and chiral Néel domain walls. These chiral structures offer perspectives for applications in memory devices based on their current-induced motion in nano-devices. Controlling DMI can therefore be used to engineer the optimal DW structure (Bloch to Néel transition) for spin-torque driven domain wall motion,<sup>[33]</sup> which is of high technological relevance.

Chiral Néel domain walls also allow for high magnetic-field-driven domain wall velocities in the flow regime that can scale with the ratio  $D/M_s$ .<sup>[34,35]</sup> In the present case, a maximum velocity plateau is observed and its maximum velocity value increases with the temperature and the annealing time as shown in Figure 5a. However, a direct correlation between this maximum velocity plateau with the values of  $D/M_s$  is not straightforward. It has been shown that the velocity plateau that has a relation with  $D/M_s$  has a high-field limit close to the DMI field  $\mu_0 H_{\text{DMI}}$ .<sup>[35,36]</sup> The  $\mu_0 H_{\text{DMI}}$  values have been measured in samples S1 to S4 by asymmetric bubble domain expansion under an in-plane magnetic field ( $\mu_0 H_x$ , see Section S5, Supporting Information) and are shown in Figure 5b–e. The velocity of right and left propagating DWs are shown as red circles and black squares, respectively. The values of  $\mu_0 H_{\text{DMI}}$  correspond to the field at which the minimum velocity is observed, and are

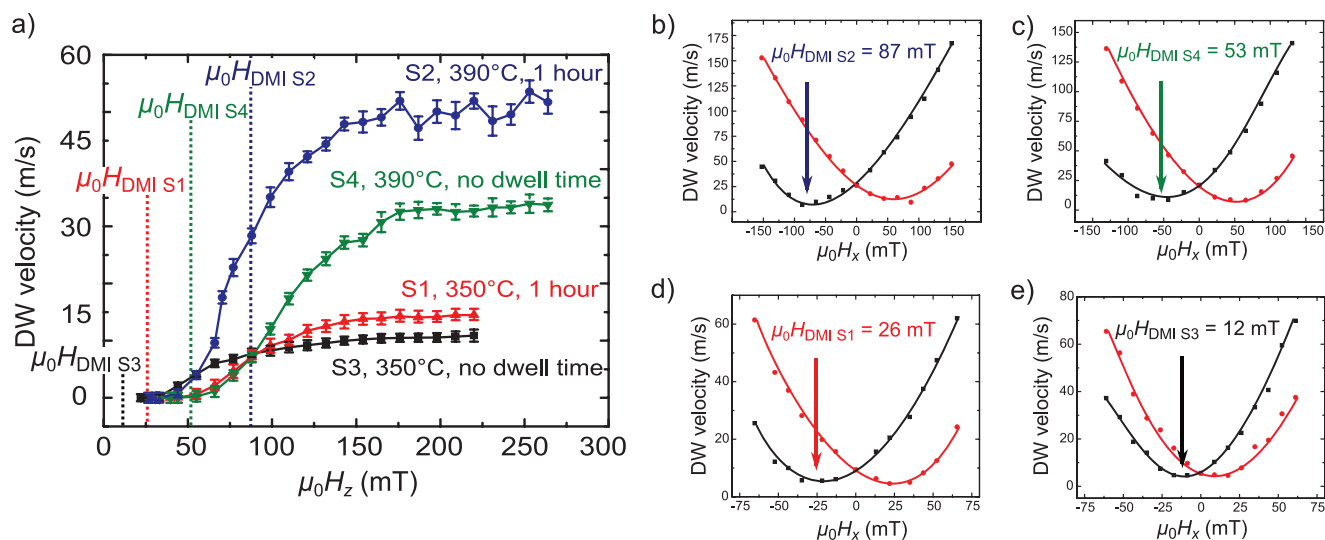


**Figure 5.** a) Magnetic DW velocity measured under an out-of-plane magnetic field ( $\mu_0 H_z$ ) for samples annealed at 350 and 390 °C for 1 h (S1, S2, respectively) and zero dwell time (S3, S4, respectively). The error bars correspond to the standard error over ten measurements on different domains. b–e) Magnetic DW velocity measured under in-plane magnetic fields ( $\mu_0 H_x$ ). Right propagating DWs are shown in red circles and left propagating DWs are shown as black squares. The values of  $\mu_0 H_{DMI}$  are indicated for all samples. Lines correspond to second order polynomial fittings.

$12 \pm 0.5$ ,  $26 \pm 1.3$ ,  $53 \pm 2.6$ , and  $87 \pm 4.3$  mT for S3, S1, S4, and S2, respectively. When these values are confronted with the velocity plots in Figure 5a, it is observed that for all the samples studied, the maximum velocity plateau starts at magnetic fields higher than  $\mu_0 H_{DMI}$ . Therefore, an analysis within the model described in refs. [35,36] can not be performed. Although the increase in the maximum velocity plateau could still be qualitatively associated with the increase in the value of  $D$ , it should be considered in the context of a simultaneous increase in the crystallinity of the films. The changes in crystallinity and interface disorder can also play an important role in DW dynamics in CoFeB films that can not be accounted for by only considering the changes in magnetization, DMI, and perpendicular anisotropy.<sup>[37,38]</sup> The interplay between the changes in DMI and crystallinity add a significant degree of complexity to the interpretation of the DW dynamics in this system, which calls for a dedicated study.

### 3. Conclusion

In conclusion, we have demonstrated a non-volatile SRT from OOP to IP magnetization and a manipulation of DMI done by means of voltage-controlled ion migration in annealed  $\beta$ -W/CoFeB/HfO<sub>2</sub> samples. The disparity in reversibility for different annealing profiles and temperatures has been linked to a difference in the degree of crystallization in W/CoFeB that can greatly affect the density of ionic conduction channels and therefore, the mobility of ions. In addition, we also showed the influence of different annealing conditions on domain wall velocity. These results provide an insight into the magneto-ionic response of systems that require annealing to enhance their magnetic properties such as PMA and DMI and point at the need of a compromise between the enhancement of magnetic properties and the magneto-ionic reversibility. The large and permanent magneto-ionic effects seen in samples

annealed at 390 °C, exhibiting strong PMA and DMI, can be of interest even in the absence of reversibility. Magneto-ionics can provide in this case a simple post-growth means to fine tune magnetic properties in a local and non-volatile fashion. This could be employed, for example, to facilitate the nucleation of skyrmions<sup>[39]</sup> or to modulate the spin-orbit torque efficiency in  $\beta$ -W/CoFeB-based spintronics devices.

### 4. Experimental Section

**Sample Preparation and Electric Field Gating:** The magnetic stack used in this study was grown using a Singulus Rotaris magnetron sputtering system. Metals (W (99.95% pure), Co<sub>20</sub>Fe<sub>60</sub>B<sub>20</sub> (99.9% pure)) were DC-sputtered and HfO<sub>2</sub> (99.9%) was RF-sputtered. Before the deposition of the film, a base pressure of  $4 \times 10^{-8}$  mbar was achieved. The deposition rate and the magnetron output power for W, Co<sub>20</sub>Fe<sub>60</sub>B<sub>20</sub>, and HfO<sub>2</sub>, were 0.017 nm s<sup>-1</sup> and 100 W, 0.114 nm s<sup>-1</sup> and 400 W, 0.129 nm s<sup>-1</sup> and 950 W, respectively and the sputtering gas used was Ar. The films used in this study had a single layer uniformity of 2.48%. The samples after deposition were annealed under different conditions of temperature and time (see Table 1) in a vacuum chamber at  $10^{-5}$  mbar.

E-fields were applied in devices with ionic-liquid gates. Gating was implemented by adding approximately 10  $\mu$ L of ionic-liquid (IL) [EMI]<sup>+</sup>[TFSI]<sup>-</sup> (1-ethyl-3-methylimidazolium bis(trifluoromethanesulfonyl) imide) to the surface of the magnetic films. The dimensions of the films used for each device are 10 mm  $\times$  5 mm, the electric field was applied in the center covering an area of 5 mm  $\times$  5 mm. A glass substrate coated with a 100 nm thick indium tin oxide (ITO) layer was used as the top electrode to apply the gate voltages, while the magnetic film was connected to ground. ITO was connected to the voltage source by means of a silver wire glued to the ITO-coated glass plate with an electrically conductive epoxy adhesive. Experiments were performed at room temperature on samples cut from the same wafer and all magnetic states presented here are non-volatile.

**Magneto-Optical Measurements:** The hysteresis loops and domain wall dynamics measurements were obtained by polar magneto-optical Kerr effect using a Zeiss Axio Imager A2m microscope. The MOKE hysteresis loops were normalized to  $\pm 1$  at saturation.

**Magnetometry Measurements:** Magnetic moment was measured by vibrating sample magnetometry using a customized DMS system.

**Brillouin Light Scattering:** The interfacial DMI was characterized using BLS. BLS was measured in the Damon–Eshbach geometry and DMI was extracted by analyzing the frequency asymmetry  $\Delta F$  between the Stokes and anti-Stokes inelastic scattering peaks as a function of the spin-wave wave vector  $k$  under an in-plane saturating magnetic field of 1 T for S2 in the initial state and 0.9 T for all the other samples (see the Section S4, Supporting Information). The relation between  $\Delta F$  and  $k$  is as follows:

$$\Delta F = \frac{2\gamma}{\pi M_s} Dk, \quad (1)$$

where  $\gamma$  and  $M_s$  are the gyromagnetic ratio and the saturation magnetization, respectively.

**X-Ray Photoelectron Spectroscopy:** XPS was performed using a PHI ESCA 5600 (PHI Electronics) apparatus equipped with a monochromatic Al K $\alpha$  X-ray source (1486.6 eV) and a hemispherical analyzer, with pass energy equal to 57.80 eV and energy resolution 0.125 eV. The XPS peak fitting shown in Figure 3 was conducted using pseudo Voigt functions and a Shirley + linear background.

**Domain Wall Motion and Asymmetric Bubble Expansion:** The domain wall (DW) motion under perpendicular and in-plane magnetic field was measured in continuous films using pMOKE microscopy. To measure the domain wall velocity under perpendicular fields ( $\mu_0 H_z$ , Figure 5a), the films were first saturated in the out-of-plane direction, and then using a 200  $\mu\text{m}$ -diameter coil placed on the surface of the film, bubble domains were nucleated with magnetic field pulses applied in the opposite direction with respect to the saturation direction. The DW velocities were calculated as the expansion of the initial bubble domain over the pulse width of the applied magnetic field.

The DW velocity as a function of the in-plane magnetic field  $\mu_0 H_x$  (see Section S5, Supporting Information) was used to determine the effective DMI field ( $\mu_0 H_{\text{DMI}}$ ) of the samples annealed under different conditions (Figure 5b–e). An identical method as the one described earlier was used to generate bubble domains. In this case, a perpendicular field pulse of fixed magnitude was applied simultaneously to the application of a constant in-plane magnetic field. The perpendicular fields  $\mu_0 H_z$  applied were 66, 99, 121, and 88 mT, for S3, S1, S4, and S2, respectively. The error in the values of  $\mu_0 H_{\text{DMI}}$  corresponded to the relative standard error from the fitting.

## Supporting Information

Supporting Information is available from the Wiley Online Library or from the author.

## Acknowledgements

The authors gratefully acknowledge financial support from the European Union H2020 Program (MSCA ITN 860060), the French National Research Agency (BIOICE), PHC Sakura and the JSPS KAKENHI grant (20H05304). This work was also partly supported by the French RENATECH network. R.P. and L.H.D. wish to thank S. Pizzini for help with DW measurements and their interpretation, A. Solignac for help with vibrating sample magnetometry and C. Lidig for sample uniformity measurements.

## Conflict of Interest

The authors declare no conflict of interest.

## Data Availability Statement

The data that support the findings of this study are available from the corresponding author upon reasonable request.

## Keywords

annealing, Dzyaloshinskii-Moriya interaction, magneto-ionics, magneto-ionic reversibility

Received: March 28, 2022

Revised: June 1, 2022

Published online:

- [1] T. Maruyama, Y. Shiota, T. Nozaki, K. Ohta, N. Toda, M. Mizuguchi, A. A. Tulapurkar, T. Shinjo, M. Shiraishi, S. Mizukami, Y. Ando, Y. Suzuki, *Nat. Nanotechnol.* **2009**, *4*, 158.
- [2] A. Bernard-Mantel, L. Herrera-Diez, L. Ranno, S. Pizzini, J. Vogel, D. Givord, S. Auffret, O. Boulle, I. M. Miron, G. Gaudin, *Appl. Phys. Lett.* **2013**, *102*, 122406.
- [3] Y. T. Liu, S. Ono, G. Agnus, J.-P. Adam, S. Jaiswal, J. Langer, B. Ocker, D. Ravelosona, L. Herrera Diez, *J. Appl. Phys.* **2017**, *122*, 133907.
- [4] T. Srivastava, M. Schott, R. Juge, V. Křížáková, M. Belmeguenai, Y. Roussigné, A. Bernard-Mantel, L. Ranno, S. Pizzini, S.-M. Chérif, A. Stashkevich, S. Auffret, O. Boulle, G. Gaudin, M. Chshiev, C. Baraduc, H. Béa, *Nano Lett.* **2018**, *18*, 4871.
- [5] T. Koyama, Y. Nakatani, J. Ieda, D. Chiba, *Sci. Adv.* **2018**, *4*, eaav0265.
- [6] S. Zhang, *Phys. Rev. Lett.* **1999**, *83*, 640.
- [7] M. Nichterwitz, S. Honnali, M. Kutuzau, S. Guo, J. Zehner, K. Nielsch, K. Leistner, *APL Mater.* **2021**, *9*, 030903.
- [8] U. Bauer, L. Yao, A. J. Tan, P. Agrawal, S. Emori, H. L. Tuller, S. van Dijken, G. S. D. Beach, *Nat. Mater.* **2015**, *14*, 174.
- [9] U. Bauer, S. Emori, G. S. D. Beach, *Nat. Nanotechnol.* **2013**, *8*, 411.
- [10] A. J. Tan, M. Huang, C. O. Avci, F. Büttner, M. Mann, W. Hu, C. Mazzoli, S. Wilkins, H. L. Tuller, G. S. D. Beach, *Nat. Mater.* **2019**, *18*, 35.
- [11] L. Herrera Diez, Y. Liu, D. Gilbert, M. Belmeguenai, J. Vogel, S. Pizzini, E. Martinez, A. Lamperti, J. Mohammedi, A. Laborieux, Y. Roussigné, A. Grutter, E. Arenholtz, P. Quarterman, B. Maranville, S. Ono, M. S. E. Hadri, R. Tolley, E. Fullerton, L. Sanchez-Tejerina, A. Stashkevich, S. Chérif, A. Kent, D. Querlioz, J. Langer, B. Ocker, D. Ravelosona, *Phys. Rev. Appl.* **2019**, *12*, 034005.
- [12] R. Mishra, F. Mahfouzi, D. Kumar, K. Cai, M. Chen, X. Qiu, N. Kioussis, H. Yang, *Nat. Commun.* **2019**, *10*, 248.
- [13] J. de Rojas, A. Quintana, A. Lopeandía, J. Salguero, B. Muñiz, F. Ibrahim, M. Chshiev, A. Nicolenco, M. O. Liedke, M. Butterling, A. Wagner, V. Sireus, L. Abad, C. J. Jensen, K. Liu, J. Nogués, J. L. Costa-Krämer, E. Menéndez, J. Sort, *Nat. Commun.* **2020**, *11*, 5871.
- [14] A. Fassatoui, J. P. Garcia, L. Ranno, J. Vogel, A. Bernard-Mantel, H. Béa, S. Pizzini, S. Pizzini, *Phys. Rev. Appl.* **2020**, *14*, 064041.
- [15] R. Pachat, D. Ourdani, J. van der Jagt, M.-A. Syskaki, A. Di Pietro, Y. Roussigné, S. Ono, M. Gabor, M. Chérif, G. Durin, J. Langer, M. Belmeguenai, D. Ravelosona, L. H. Diez, *Phys. Rev. Appl.* **2021**, *15*, 064055.
- [16] A. Fassatoui, L. Ranno, J. PeñaGarcia, C. Balan, J. Vogel, H. Béa, S. Pizzini, *Small* **2021**, *17*, 2102427.
- [17] B. Dieny, M. Chshiev, *Rev. Mod. Phys.* **2017**, *89*, 025008.
- [18] G. W. Kim, A. S. Samardak, Y. J. Kim, I. H. Cha, A. V. Ogniev, A. V. Sadovnikov, S. A. Nikitov, Y. K. Kim, *Phys. Rev. Appl.* **2018**, *9*, 064005.
- [19] K. Garello, F. Yasin, G. S. Kar, in *2019 IEEE 11th Int. Memory Workshop (IMW)*, IEEE, Piscataway, NJ **2019**, pp. 1–4.
- [20] A. Ghosh, H. J. Chung, K. H. Khoo, J. Shanmugam, J. Qiu, S. Allauddin, S. T. Lim, *Adv. Electron. Mater.* **2022**, *8*, 2100982.
- [21] G.-G. An, J.-B. Lee, S.-M. Yang, J.-H. Kim, W.-S. Chung, J.-P. Hong, *Acta Mater.* **2015**, *87*, 259.

- [22] K.-U. Demasius, T. Phung, W. Zhang, B. P. Hughes, S.-H. Yang, A. Kellock, W. Han, A. Pushp, S. S. P. Parkin, *Nat. Commun.* **2016**, 7, 10644.
- [23] A. Manchon, C. Ducruet, L. Lombard, S. Auffret, B. Rodmacq, B. Dieny, S. Pizzini, J. Vogel, V. Uhlir, M. Hochstrasser, G. Panaccione, *J. Appl. Phys.* **2008**, 104, 043914.
- [24] W. Skowroński, T. Nozaki, D. D. Lam, Y. Shiota, K. Yakushiji, H. Kubota, A. Fukushima, S. Yuasa, Y. Suzuki, *Phys. Rev. B* **2015**, 91, 184410.
- [25] S. Jaiswal, K. Litzius, I. Lemesh, F. Büttner, S. Finizio, J. Raabe, M. Weigand, K. Lee, J. Langer, B. Ocker, G. Jakob, G. S. D. Beach, M. Kläui, *Appl. Phys. Lett.* **2017**, 111, 022409.
- [26] S. S. K. Kalal, H. P. Perumal, D. Kumar, M. Gupta, J. Sinha, *Mater. Sci. Eng., B* **2021**, 272, 115367.
- [27] B. J. Tan, K. J. Klabunde, P. M. A. Sherwood, *Chem. Mater.* **1990**, 2, 186.
- [28] B. J. Tan, K. J. Klabunde, P. M. A. Sherwood, *J. Am. Chem. Soc.* **1991**, 113, 855.
- [29] D. Sarma, C. Rao, *J. Electron Spectrosc. Relat. Phenom.* **1980**, 20, 25.
- [30] C. D. Wagner, D. A. Zatko, R. H. Raymond, *Anal. Chem.* **1980**, 52, 1445.
- [31] X. D. Xu, K. Mukaiyama, S. Kasai, T. Ohkubo, K. Hono, *Acta Mater.* **2018**, 161, 360.
- [32] D. A. Gilbert, A. J. Grutter, E. Arenholz, K. Liu, B. J. Kirby, J. A. Borchers, B. B. Maranville, *Nat. Commun.* **2016**, 7, 12264.
- [33] A. V. Khvalkovskiy, V. Cros, D. Apalkov, V. Nikitin, M. Krounbi, K. A. Zvezdin, A. Anane, J. Grollier, A. Fert, *Phys. Rev. B* **2013**, 87, 020402.
- [34] T. Ha Pham, J. Vogel, J. Sampaio, M. Vaňatka, J.-C. Rojas-Sánchez, M. Bonfim, D. S. Chaves, F. Choueikani, P. Ohresser, E. Otero, A. Thiaville, S. Pizzini, *Europhys. Lett.* **2016**, 113, 67001.
- [35] V. Krizakova, J. P. Garcia, J. Vogel, N. Rougemaille, D. d. S. Chaves, S. Pizzini, A. Thiaville, *Phys. Rev. B* **2019**, 100, 214404.
- [36] J. P. Garcia, A. Fassatoui, M. Bonfim, J. Vogel, A. Thiaville, S. Pizzini, *Phys. Rev. B* **2021**, 104, 014405.
- [37] C. Burrowes, N. Vernier, J.-P. Adam, L. Herrera Diez, K. Garcia, I. Barisic, G. Agnus, S. Eimer, J.-V. Kim, T. Devolder, A. Lamperti, R. Mantovan, B. Ockert, E. E. Fullerton, D. Ravelosona, *Appl. Phys. Lett.* **2013**, 103, 182401.
- [38] L. H. Diez, M. Voto, A. Casiraghi, M. Belmeguenai, Y. Roussigné, G. Durin, A. Lamperti, R. Mantovan, V. Sluka, V. Jeudy, Y. T. Liu, A. Stashkevich, S. M. Chérif, J. Langer, B. Ocker, L. Lopez-Diaz, D. Ravelosona, *Phys. Rev. B* **2019**, 99, 054431.
- [39] K.-W. Moon, S. Yang, T.-S. Ju, C. Kim, B. S. Chun, S. Park, C. Hwang, *NPG Asia Mater.* **2021**, 13, 20.